

# Integration of Microstructural Image Data into Machine Learning Models for Advancing High-Performance Perovskite Solar Cell Design

Haotian Liu,<sup>#</sup> Antai Yang,<sup>#</sup> Chengquan Zhong,<sup>#</sup> Xu Zhu, Hao Meng, Zuo Feng, Jixin Tang, Chen Yang, Jingzi Zhang,\* Jiakai Liu,\* Kailong Hu,\* and Xi Lin\*



Cite This: *ACS Energy Lett.* 2025, 10, 1884–1891



Read Online

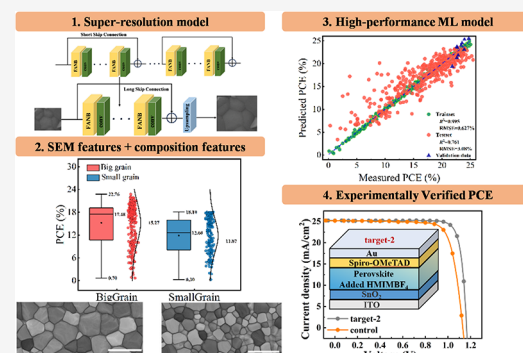
## ACCESS |

Metrics & More

Article Recommendations

Supporting Information

**ABSTRACT:** Perovskite microstructure is one of the key factors limiting the effectiveness of current machine learning (ML) approaches for designing perovskite solar cells (PSCs) with high power conversion efficiency (PCE). This work develops a multimodal convolutional neural network to extract microstructural features from scanning electron microscopy (SEM) images of perovskite thin films. The model dynamically adjusts the weights of different modal information, including material composition, processing techniques, and microstructure, to enhance predictive accuracy. The model achieves an impressive coefficient of determination ( $R^2$ ) of 0.79 on the 1,583 SEM images data set. By introducing six SEM image features to describe the grain size of PSCs, we found that a grain boundary length density (GBLD) below 5.96 and an equivalent circular diameter (ECD) above 0.83 significantly enhance the PCE. Additional experiments confirmed the effectiveness of the results, and by improving these parameters to alter the crystallization, the PCE was increased to 24.61%, and the consistency of the results demonstrated the effectiveness and rationality of the multimodal model.



The power conversion efficiency (PCE) of perovskite solar cells (PSCs) depends on multiple factors, including material composition, device structure, and fabrication techniques.<sup>1–6</sup> In recent years, machine learning (ML) has been proven to be a powerful tool for accelerating experimental processes and understanding the relationship between PSCs and their performance.<sup>7–11</sup> In previous research, good progress has been made in using manually defined features to predict PCE,<sup>9,10</sup> however, slight variations in experimental factors such as the quality of precursor materials, the ambient environment, the humidity and temperature, and the uncontrollability of each operation step can lead to different quality of perovskite film formation.<sup>12–15</sup> The difficulty of quantitatively monitoring these factors is the primary factor restricting the further improvement of PCE prediction accuracy.<sup>16,17</sup> Understanding the changes in the film quality and crystallization status of perovskite films is the key to revealing the internal laws of PSCs and improving the accuracy of PCE prediction.<sup>18–20</sup>

This work introduces a multimodal prediction framework to address the limitations of traditional ML algorithms in accurately predicting material performance by integrating material composition, microstructural features from scanning

electron microscopy (SEM) images, and processing techniques. Integrating SEM images enhances the model's precision by providing detailed microstructural insights.<sup>21</sup> On the prediction task of PCE, the multimodal model markedly outperforms the unimodal model, achieving an impressive coefficient of determination ( $R^2$ ) of 0.79 and a root-mean-square error (RMSE) of 2.27. Additionally, to enhance the interpretability of the model, features from SEM images were manually annotated to study the impact of grain dimensions on PCE. These features include two size indicators (equivalent circular diameter (ECD), major axis length), two shape indicators (grain boundary length density (GBLD), aspect ratio), and two uniformity indicators (standard deviation of ECD, standard deviation of aspect ratio). The model shows that when GBLD is below  $5.96 \mu\text{m}^{-1}$ , the proportion of

Received: February 26, 2025

Revised: March 19, 2025

Accepted: March 25, 2025

Published: March 26, 2025



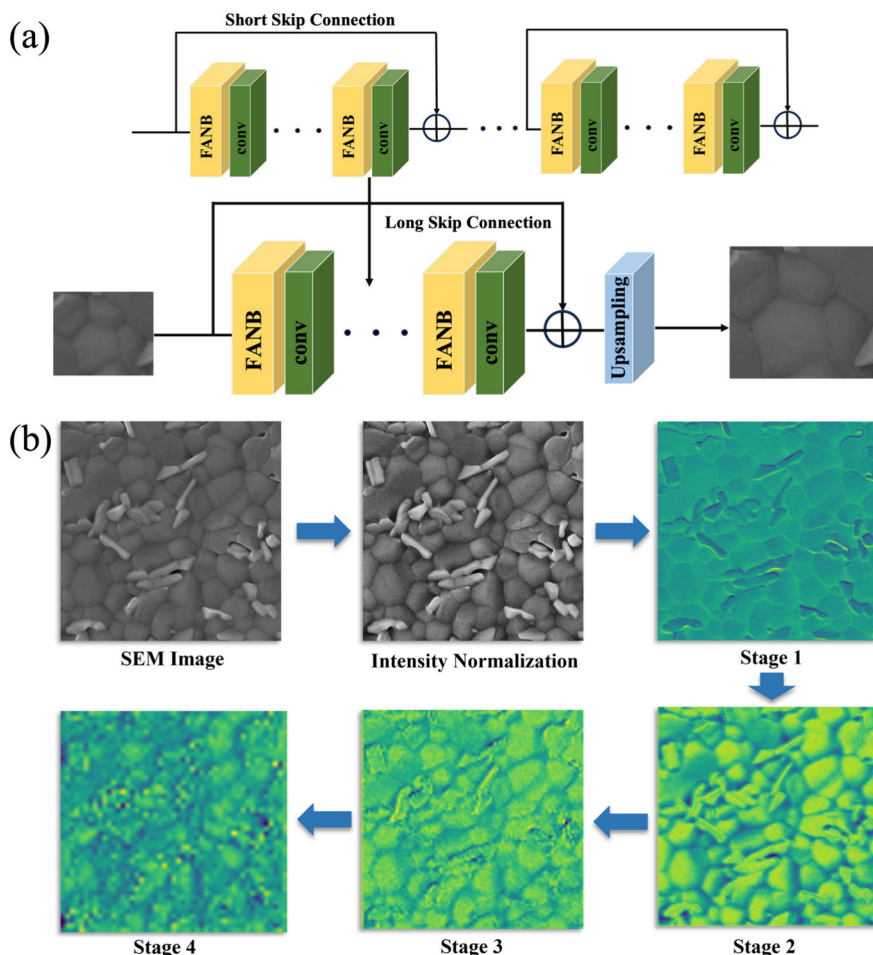


**Figure 1.** (a) Super-resolution model structure based on the frequency domain's dual-attention mechanism. (b) Feature maps extracted from different depth convolution layers.

samples with PCE > 20% increases by 9%. This highlights the importance of optimizing grain morphology to enhance PSCs performance. Experimental validation confirms that adding HMIMBF<sub>4</sub> ionic liquid increases ECD and reduces GBLD, boosting PCE from 22.09% to 24.61%.

A total of 1,892 data points from 623 published articles (2015–2023) were compiled to construct a high-quality SEM image database. This database includes SEM images of perovskite thin films and cross-sectional views of PSCs, along with associated material and process information. The foundational data set includes material composition, manufacturing processes, and SEM images of PSCs. After data cleansing, it contains 1,892 material and process entries and 1,583 SEM images (Table S1). SEM images were resized and cropped into six equal segments to maintain critical details and aspect ratios. Image augmentation techniques, including contrast enhancement, super-resolution, and flipping, were applied to expand the data set and improve diversity. A super-resolution algorithm Swin Transformer for Image Restoration (SWINIR) was used to enhance grain boundary clarity (Figure S1),<sup>22</sup> with results evaluated using Peak Signal-to-Noise Ratio (PSNR) and Structural Similarity Index Measure (SSIM) metrics (Tables S2 and S3).<sup>23</sup> The final data set expanded to 76,584 images for training a deep learning model.

A frequency-domain dual attention mechanism was integrated into the SEM image feature extraction network of the convolutional neural network (CNN),<sup>24,25</sup> allowing the

model to focus on critical areas for accurate predictions (Figure 1a). Due to the varied effects of different modalities (e.g., component ratio and microstructure) on PSCs performance, direct fusion can introduce bias.<sup>26</sup> Therefore, an adaptive feature vector fusion module was designed to automatically learn the weights of different modal information during training, enhancing model interpretability and robustness. A multilayer perceptron (MLP) with one hidden layer was then used as the regression predictor to forecast PSCs performance based on the fused feature vector. This end-to-end model enables training and prediction of PSCs performance.<sup>27</sup> Figure 1b shows feature maps from five stages, illustrating that lower-level layers capture basic features (e.g., edges) while higher-level layers extract more complex features (e.g., grain shapes). The prediction model integrates diverse data sources to improve accuracy and consists of three components: feature extraction, feature fusion, and regression prediction. Model details are provided in Table S4, Table S5, and Figure S2. The image feature extraction network uses high-resolution SEM images to identify microstructural features like grain size and morphology. Adaptive histogram normalization is applied to enhance image contrast and detail (Figure S3). The model then fuses material, process, and SEM image features using an adaptive fusion module for comprehensive PCE predictions.

The data set was divided into 80% for training and 20% for testing. Figure S4 shows the 10-fold cross-validation performance of five models: MLP,<sup>28</sup> Support Vector Regression

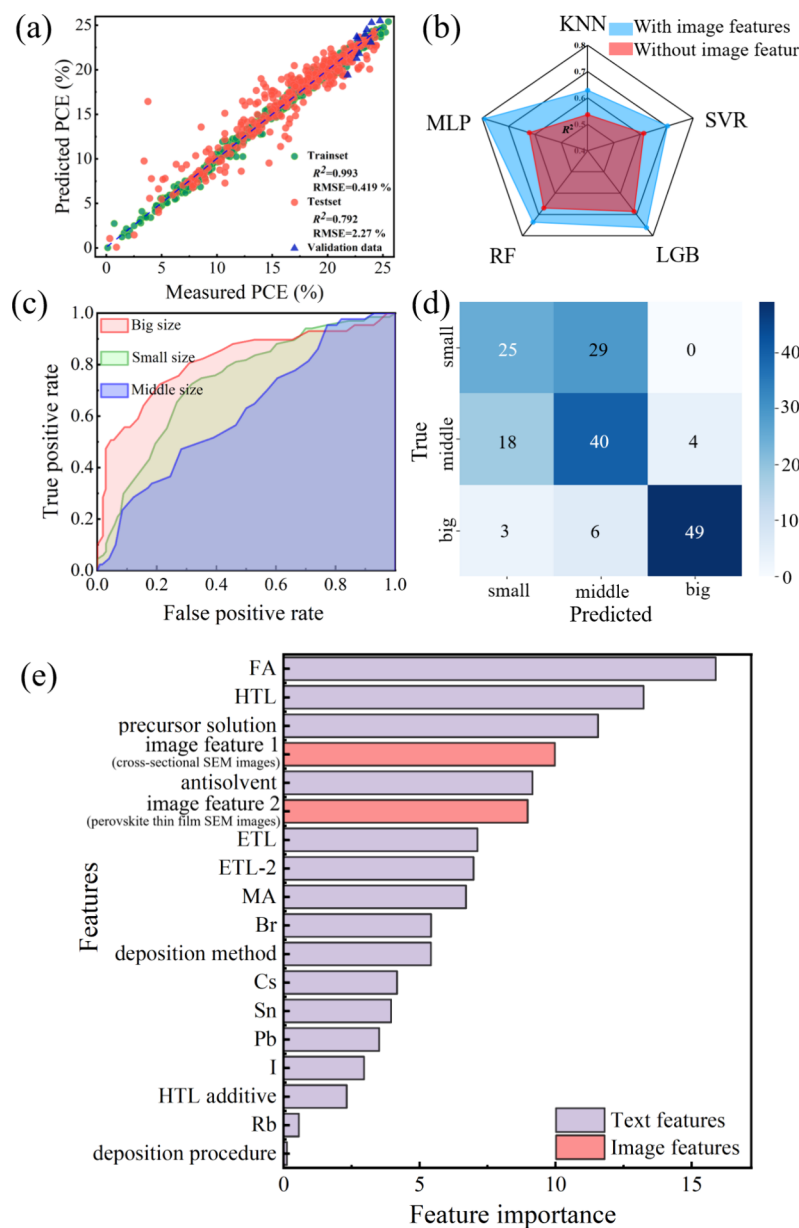


**Figure 2.** (a) Fitted PCE results of the MLP model, with the training set represented in green and the test set in red. (b) Comparison of  $R^2$  values for models with and without the inclusion of image features. (c) ROC curve, with red representing big-sized grains, green representing small-sized grains, and blue representing middle-sized grains. (d) Confusion matrix. (e) Features importance in the multimodal fusion model.

(SVR),<sup>29</sup> LightGBM (LGB),<sup>30</sup> Random Forest (RF),<sup>31</sup> and K-Nearest Neighbors (KNN).<sup>32</sup> The detailed list of the five model hyperparameters is in Table S6. The MLP model performed best in  $R^2$  and RMSE. Figure 2a indicates that the multimodal fusion model using MLP achieved the highest performance with an  $R^2$  of 0.792 and an RMSE of 2.27% on the test set. The regression scatter plots of the other four models are provided in Figure S5. Triangular markers in Figure 2a represent experimental data from 2024 articles, excluded from the original data set, demonstrating the model's accuracy and generalization ability. Figure 2b compares  $R^2$  values for models with and without image features, highlighting the importance of image data. The classification model is based on the CNN and employs the Visual Geometry Group (VGG) architecture. The model's input solely consists of annotated perovskite thin film SEM images. Figure 2c shows the receiver

operating characteristic (ROC) curves for different grain sizes, with area under curve (AUC) values of 0.826, 0.768, and 0.657 for big, small, and middle grains, respectively. Figure 2d confirms the model's high true positive rate for big grains, indicating effective feature extraction and grain size classification. The detailed list of the CNN model hyperparameters is in Table S7.

Figure 2e shows the feature importance of the multimodal fusion model. The content of formamidinium (FA) in the perovskite layer, the material for the hole transport layer (HTL), and the precursor solution are the most important features for PCE prediction. SEM image features (cross-sectional SEM images and perovskite thin film SEM images) are ranked fourth and sixth, respectively. The models delve into the prediction analysis of PCE by investigating the influence of various factors, including the microstructural

**Table 1.** PCE Prediction Performance of Different Models with Various Input Feature Types and Numbers

feature type <sup>a</sup>	number of features	metrics	MLP	SVR	LGB	RF	KNN
Ma	14	RMSE	3.61	3.23	<b>3.11</b>	3.49	4.32
		$R^2$	0.523	0.574	<b>0.641</b>	0.541	0.489
Ma+Pr	21	RMSE	3.89	3.48	<b>2.92</b>	3.80	3.55
		$R^2$	0.621	0.613	<b>0.685</b>	0.669	0.537
Ma+Pr+S1	53	RMSE	3.43	2.65	<b>2.26</b>	2.39	3.16
		$R^2$	0.703	0.663	<b>0.714</b>	0.697	0.605
Ma+Pr+S2	53	RMSE	2.57	3.19	<b>2.41</b>	3.47	3.74
		$R^2$	0.712	0.643	<b>0.747</b>	0.728	0.593
S1+S2	64	RMSE	<b>3.83</b>	4.82	4.10	4.24	4.5
		$R^2$	<b>0.401</b>	0.265	0.366	0.352	0.335
Ma+Pr+S1+S2	85	RMSE	<b>2.27</b>	2.83	3.08	2.59	3.34
		$R^2$	<b>0.792</b>	0.703	0.761	0.735	0.629

<sup>a</sup>Ma represents material composition features, Pr represents processing methods features, S1 represents features extracted from perovskite thin film SEM images, and S2 represents features extracted from cross-sectional SEM images of PSCs.

**Table 2.** Comparison of the Predicted and Experimentally Measured PCE Values for Reported PSCs Assembled Using the Various Perovskite Materials

sample number	perovskite	ETL	ETL-2	HTL	HTL additive	predicted PCE	measured PCE
1 <sup>37</sup>	FAPbI <sub>3</sub>	SnO <sub>2</sub>	no	p-A5HP-E-POZOD-E	no	24.73	25.5
2 <sup>38</sup>	FAPbI <sub>3</sub>	c-TiO <sub>2</sub>	SnO <sub>2</sub>	MF-ACD	no	23.91	23.1
3 <sup>39</sup>	FA <sub>0.85</sub> MA <sub>0.1</sub> Cs <sub>0.05</sub> PbI <sub>3</sub>	BCP	C <sub>60</sub>	MeO-2PACZ	no	23.54	24.51
4 <sup>40</sup>	FA <sub>0.6</sub> MA <sub>0.4</sub> Pb <sub>0.4</sub> Sn <sub>0.6</sub> I <sub>3</sub>	SnO <sub>2</sub>	C <sub>60</sub>	4PADCB	no	22.62	21.28
5 <sup>41</sup>	MA <sub>0.27</sub> FA <sub>0.73</sub> PbI <sub>2.67</sub> Cl <sub>0.3</sub> Br <sub>0.03</sub>	SnO <sub>2</sub> -CuCl <sub>2</sub>	no	Spiro-OMeTAD	Li+TBP	22.63	23.71
6 <sup>42</sup>	FAPbI <sub>3</sub>	SnO <sub>2</sub>	no	SBF-FC	TTI	23.71	23.5
7 <sup>43</sup>	FA <sub>0.85</sub> MA <sub>0.1</sub> Cs <sub>0.05</sub> PbI <sub>3</sub>	TiO <sub>2</sub> -Zr	no	Spiro-OMeTAD	Li+TBP	20.81	19.42
8 <sup>44</sup>	FAPbI <sub>3</sub>	SnO <sub>2</sub> -PVPA	no	Spiro-OMeTAD	Li+TBP	23.83	24.0
9 <sup>45</sup>	FAPbI <sub>3</sub>	SnO <sub>2</sub> -W	no	Spiro-OMeTAD	Li+TBP	22.85	21.83
10 <sup>46</sup>	FAPbI <sub>3</sub>	SnO <sub>2</sub>	no	Spiro-OMeTAD	MSBH	23.97	25.3

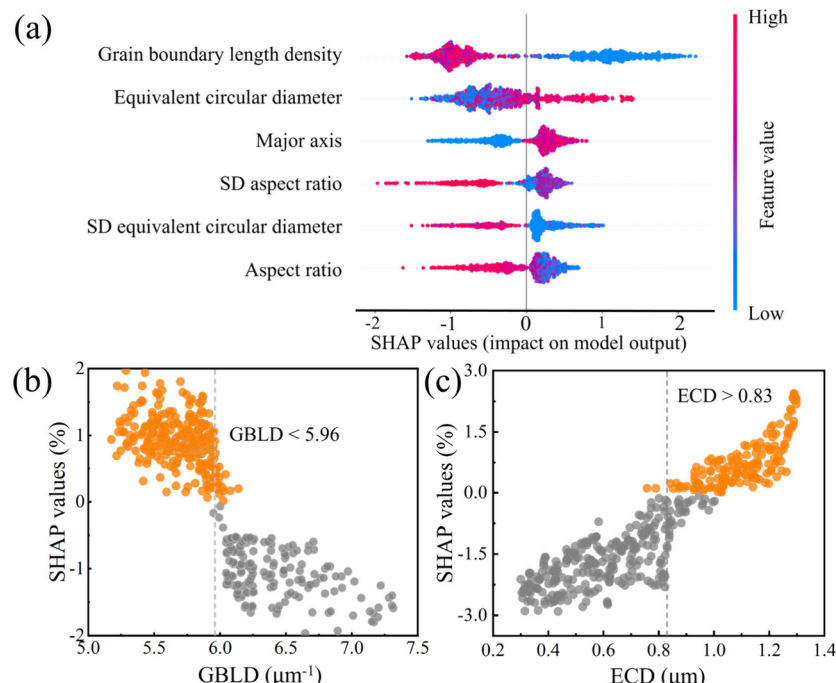


**Figure 3.** (a) SHAP value analysis plot evaluating the feature importance of features in SEM image. (b) The SHAP values for the GBLD feature in the annotated features in the SEM image data. (c) The SHAP values for the ECD feature in the SEM image data.

information extracted from cross-sectional images of PSCs. Cross-sectional SEM images reveal the thickness and quality of the perovskite layer, providing critical insights into light

absorption and charge carrier dynamics, key factors influencing PCE. If the perovskite layer is too thin, it may result in insufficient light absorption, reducing charge carriers.<sup>33,34</sup>

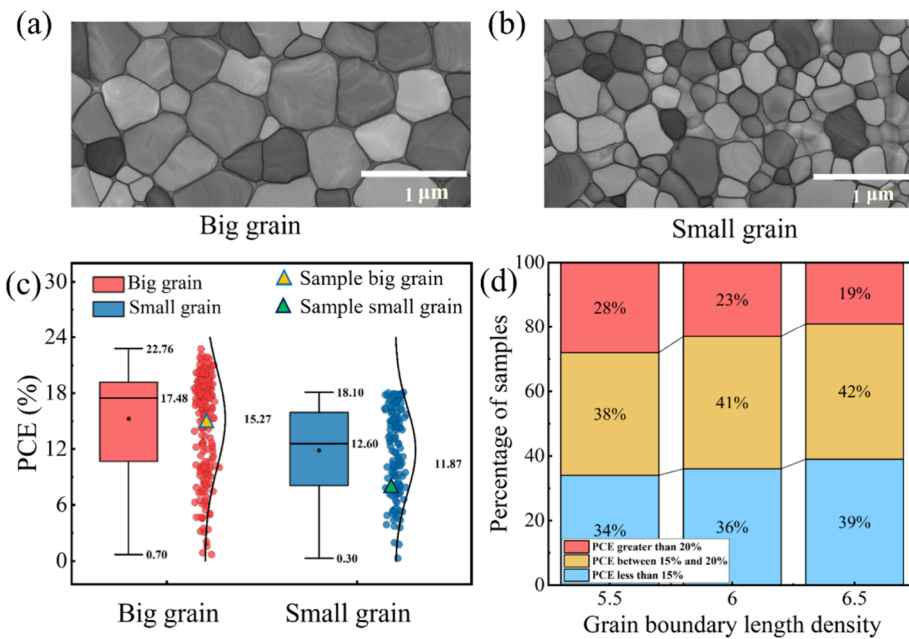


**Figure 4.** (a) SEM image sample of a big-grained perovskite thin film SEM image. (b) SEM image sample data of a small-grained perovskite thin film. (c) Box plot of PCE distribution for PSCs with big and small grain sizes. (d) Predicted PCE distribution under varying GBLD ranges.

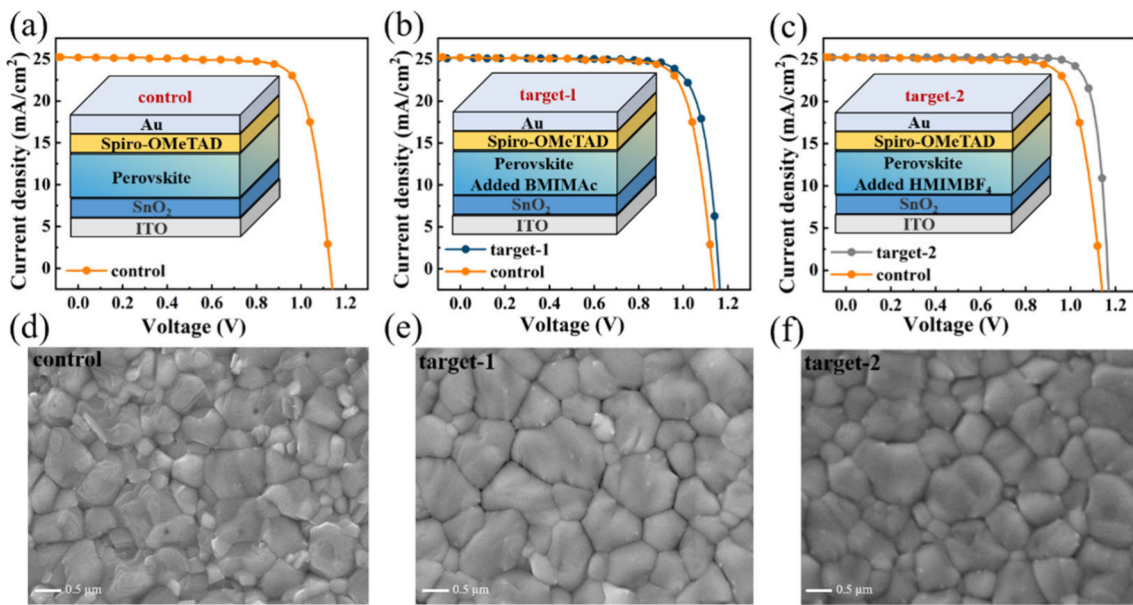
Conversely, an excessively thick perovskite layer increases the diffusion length of charge carriers, exacerbating recombination and negatively impacting the collection efficiency.<sup>35,36</sup>

Table 1 evaluates the performance of five ML models (MLP, SVR, LGB, RF, and KNN) in predicting PCE using different feature combinations. The models show varying accuracy, measured by RMSE and  $R^2$ . The trend indicates that integrating more features, especially material composition, processing methods, and microstructure characteristics, significantly improves prediction accuracy. The multimodal fusion model achieves the best performance with an  $R^2$  of 0.792 using the full feature set. Table 2 summarizes the predictive results for a subset of PSCs tested and reported in 2024 references. It provides an overview of the materials and fabrication parameters, including perovskite compositions, electron transport layer (ETL), HTL additives, and the predicted and measured PCE. The comparison with experimental results demonstrates the model's ability to accurately predict PSCs performance across various materials and processes.

SEM characterization of perovskite thin films reveals critical information about crystal size, shape, surface texture, and defects, which are closely linked to PSCs performance. Six SEM image feature factors—ECD, GBLD, major axis length, aspect ratio, and their standard deviations—are identified to quantify the relationship between microstructure and PCE. These features are extracted through image labeling and selection, enhancing the interpretability of the multimodal fusion prediction model. The detailed procedure for extracting and calculating SEM feature factors is provided in Section 3 of the Supporting Information. The LGB model was constructed using SEM features factors, material composition features, and processing method features as input, achieving an RMSE of 2.61 and an  $R^2$  of 0.727 (Figure S6). Figure 3a shows the Shapley additive explanations (SHAP) values for six key features, highlighting their importance in predicting PCE. These values quantify each feature's contribution to the

model's output, illustrating their significance in PCE prediction. GBLD is notably more significant than other shape indicators, suggesting its role as a key feature in PCE prediction. GBLD affects grain boundary distribution and the associated performance characteristics by reflecting the density of grain boundaries within a given area. Lower GBLD typically indicates a more uniform grain structure with fewer defects, which can enhance charge carrier transport and improve photonic efficiency. In contrast, features like aspect ratio provide less insight into boundary continuity or defect distribution, explaining their lower importance in the SHAP analysis. Additionally, the higher ECD aids in light scattering and absorption, thus increasing light utilization efficiency, while a lower ECD may cause local scattering losses, negatively affecting photoelectric performance. Furthermore, Figure 3b,c displays the SHAP values for PCE in the data set, further validating the impact of two significant features. Figure 3b shows that for GBLD values smaller than 5.96, the SHAP values are predominantly positive, and the predicted PCE increases as GBLD decreases. Similarly, an ECD exceeding 0.83 enhances PCE values.

Moreover, SEM images of the perovskite layer offer information on the size of perovskite grains, significantly influencing the PCE. Larger grain sizes are generally associated with improved charge transport and reduced recombination, potentially enhancing the PCE. However, the relationship between grain size and PCE is complex and can be influenced by other factors such as grain boundary properties and material defects. Figure 4a presents sample data of a big-grained perovskite thin film, while Figure 4b shows sample data of a small-grained counterpart. These images emphasize the variation in grain size, a critical parameter affecting PSCs performance. Additionally, in Figure 4c a classification model was utilized to categorize the grain size of PSCs films from 377 samples made of the  $\text{MAPbI}_3$  material. The average PCE of PSCs with bigger grain sizes has increased by 3.4%. This enhancement is attributed to the change in the grain size,



PCE predicted = 21.36% control ECD = 0.691 PCE predicted = 23.29% target-1 ECD = 0.864 PCE predicted = 24.37% target-2 ECD = 0.984  
PCE control = 22.09% control GBLD = 5.85 PCE target-1 = 22.94% target-1 GBLD = 5.47 PCE target-2 = 24.61% target-2 GBLD = 4.02

**Figure 5.** (a) Device structure and  $J$ – $V$  curve for the control. (b) Device structure of target 1 and comparison of  $J$ – $V$  curves before and after adding BMIMAc. (c) Device structure of target 2 and comparison of  $J$ – $V$  curves before and after adding HMIMBF<sub>4</sub>. (d) SEM image of the perovskite film for the control. (e) SEM image of the perovskite film for target 1. (f) SEM image of the perovskite film for target 2.

which has been identified as a crucial factor influencing PSCs performance. Figure 4d shows the use of the ML model to predict the PCE of the same PSCs and analyzes the variation in PCE distribution under different GBLD settings (5.5, 6, and 6.5). The bar chart in the figure displays the proportion of PSCs samples with PCE above 20% for each GBLD setting. It is evident that as GBLD decreases, the proportion of samples with PCE above 20% increases. When the GBLD is set to 5.5, 28% of the samples are predicted by the model to have a PCE greater than 20%, which is significantly higher than the 19% observed when the GBLD is set to 6.5. This trend suggests that GBLD plays a significant role as a shape feature affecting PCE, and reducing GBLD may be a viable approach to enhance PCE performance.

The experiment aimed to improve the film's grain morphology by adding BMIMAc and HMIMBF<sub>4</sub> ionic liquids and evaluating their impact on PSCs performance. In Figure 5, the experimental results indicate that BMIMAc (target 1) and HMIMBF<sub>4</sub> (target 2) significantly improved the grain morphology of the perovskite film. Figure 5a–c shows the device structures and  $J$ – $V$  curves for the control group, target 1, and target 2, respectively. The SEM images reveal that the addition of BMIMAc resulted in an increase in grain size and a more uniform distribution (ECD = 0.864, GBLD = 5.47). The effect of HMIMBF<sub>4</sub> (ECD = 0.984, GBLD = 4.02) was slightly better than that of BMIMAc. The variations in ECD and GBLD are consistent with the SHAP analysis, confirming the validity of the model's predictions. Specifically, the PCE increased from 22.09% to 22.94% with BMIMAc, and from 22.09% to 24.61% with HMIMBF<sub>4</sub>. As shown in Figure 5d–f, the SEM images reveal that the addition of BMIMAc and HMIMBF<sub>4</sub> led to an increase in grain size and a more uniform distribution.

The performance of PSCs is strongly affected by material composition, processing techniques, and microstructure. A high-quality data set of 1,892 material-process entries and

1,583 SEM images was developed to address these complexities, supporting a multimodal prediction model that integrates feature extraction for materials, processes, and microstructures. Using an adaptive feature fusion module, the model synthesizes diverse factors to accurately predict photovoltaic efficiency, achieving an  $R^2$  of 0.79 and an RMSE of 2.27. Six effective features characterizing the grain size of PSCs were developed. The model shows that PCE can be effectively improved when the ECD exceeds 0.83 and the GBLD is below 5.96. The rationality and effectiveness of the framework have been verified through multiple experiments, with the PCE enhanced to 24.61%. This work highlights the importance of multimodal information fusion in the PSCs design, demonstrating how the model integrates microstructure, composition, processing, and performance data to enhance predictive capability and accelerate innovation in PSCs technology. Moreover, this framework has great potential for application in predicting performance and explaining mechanisms in other materials and devices.

## ASSOCIATED CONTENT

### Supporting Information

The Supporting Information is available free of charge at <https://pubs.acs.org/doi/10.1021/acsenergylett.5c00626>.

Additional details of the perovskite thin film microstructure feature extraction network, composition and processing feature extraction network, convolutional neural network, regression models, classification models, and adaptive feature fusion method; the procedure for extracting and calculating SEM features; additional experimental details, materials, and device fabrication (PDF)

## AUTHOR INFORMATION

### Corresponding Authors

Jingzi Zhang – School of Materials Science and Engineering and School of Computer Science and Technology, Harbin Institute of Technology, Shenzhen 518055, China; Email: [zjzhang@hit.edu.cn](mailto:zjzhang@hit.edu.cn)

Jiakai Liu – Xinjiang Key Laboratory of Separation Material and Technology, Xinjiang Technical Institute of Physics and Chemistry, Chinese Academy of Sciences, Urumqi 830011, China; Center of Materials Science and Opto-electronic Technology, University of Chinese Academy of Sciences, Beijing 100049, China; Email: [liujk@ms.xjb.ac.cn](mailto:liujk@ms.xjb.ac.cn)

Kailong Hu – School of Materials Science and Engineering, Harbin Institute of Technology, Shenzhen 518055, China; [ORCID: 0000-0003-0489-5836](https://orcid.org/0000-0003-0489-5836); Email: [hukailong@hit.edu.cn](mailto:hukailong@hit.edu.cn)

Xi Lin – School of Materials Science and Engineering, Harbin Institute of Technology, Shenzhen 518055, China; [ORCID: 0000-0003-3937-0570](https://orcid.org/0000-0003-3937-0570); Email: [linxi@hit.edu.cn](mailto:linxi@hit.edu.cn)

### Authors

Haotian Liu – School of Materials Science and Engineering, Harbin Institute of Technology, Shenzhen 518055, China

Antai Yang – School of Materials Science and Engineering, Harbin Institute of Technology, Shenzhen 518055, China

Chengquan Zhong – School of Materials Science and Engineering, Harbin Institute of Technology, Shenzhen 518055, China; [ORCID: 0000-0001-7409-3367](https://orcid.org/0000-0001-7409-3367)

Xu Zhu – School of Materials Science and Engineering, Harbin Institute of Technology, Shenzhen 518055, China

Hao Meng – School of Materials Science and Engineering, Harbin Institute of Technology, Shenzhen 518055, China

Zhuo Feng – School of Materials Science and Engineering, Harbin Institute of Technology, Shenzhen 518055, China

Jixin Tang – School of Materials Science and Engineering, Harbin Institute of Technology, Shenzhen 518055, China

Chen Yang – Xinjiang Key Laboratory of Separation Material and Technology, Xinjiang Technical Institute of Physics and Chemistry, Chinese Academy of Sciences, Urumqi 830011, China

Complete contact information is available at:

<https://pubs.acs.org/10.1021/acsenergylett.5c00626>

### Author Contributions

#H.L., A.Y., and C.Z. contributed equally to this work. Conceptualization: H.L., A.Y., C.Z., X.L. Experiments: X.Z., H.M., Z.F., J.T., C.Y. Manuscript writing: H.L., J.Z., J.L., K.H., X.L. Project Coordination: X.L., J.L.

### Notes

The authors declare no competing financial interest.

## ACKNOWLEDGMENTS

The authors appreciate financial support from the Guangdong Basic and Applied Basic Research Foundation (2022A1515110676, 2024A1515011845), the Shenzhen Science and Technology Program (JCYJ20220531095404009; JCYJ20230807094313028), Tianchi Talent Program (Grant No.: E439630301), and the Project Supported by Sunrise (Xiamen) Photovoltaic Industry Co., Ltd. (Development of Artificial Intelligence Technology for Perovskite Photovoltaic Materials, No. HX20230176).

## REFERENCES

- (1) Liu, P.; Han, N.; Wang, W.; Ran, R.; Zhou, W.; Shao, Z. High-Quality Ruddlesden-Popper Perovskite Film Formation for High-Performance Perovskite Solar Cells. *Adv. Mater.* **2021**, *33*, No. 2002582.
- (2) Zhang, X.; Yang, T.; Ren, X.; Zhang, L.; Zhao, K.; Liu, S. Film Formation Control for High Performance Dion-Jacobson 2d Perovskite Solar Cells. *Adv. Energy Mater.* **2021**, *11*, No. 2002733.
- (3) Chao, L.; Niu, T.; Gao, W.; Ran, C.; Song, L.; Chen, Y.; Huang, W. Solvent Engineering of the Precursor Solution toward Large-Area Production of Perovskite Solar Cells. *Adv. Mater.* **2021**, *33*, No. 2005410.
- (4) Sun, S.; Lu, M.; Gao, X.; Shi, Z.; Bai, X.; Yu, W. W.; Zhang, Y. 0D Perovskites: Unique Properties, Synthesis, and Their Applications. *Adv. Sci.* **2021**, *8*, No. 2102689.
- (5) Liu, S.; Li, J.; Xiao, W.; Chen, R.; Sun, Z.; Zhang, Y.; Lei, X.; Hu, S.; Kober-Czerny, M.; Wang, J. Buried Interface Molecular Hybrid for Inverted Perovskite Solar Cells. *Nature* **2024**, *632*, 536–542.
- (6) Zhu, P.; Wang, D.; Zhang, Y.; Liang, Z.; Li, J.; Zeng, J.; Zhang, J.; Xu, Y.; Wu, S.; Liu, Z. Aqueous Synthesis of Perovskite Precursors for Highly Efficient Perovskite Solar Cells. *Science* **2024**, *383*, 524–531.
- (7) Zhang, X.; Ding, B.; Wang, Y.; Liu, Y.; Zhang, G.; Zeng, L.; Yang, L.; Li, C.-J.; Yang, G.; Nazeeruddin, M. K.; Chen, B. Machine Learning for Screening Small Molecules as Passivation Materials for Enhanced Perovskite Solar Cells. *Adv. Funct. Mater.* **2024**, *34*, No. 2314529.
- (8) Paraskeva, V.; Norton, M.; Livera, A.; Kyrianiou, A.; Hadjipanayi, M.; Peraticos, E.; Aguirre, A.; Ramesh, S.; Merckx, T.; Ebner, R.; Aernouts, T.; Krishna, A.; Georghiou, G. E. Diurnal Changes and Machine Learning Analysis of Perovskite Modules Based on Two Years of Outdoor Monitoring. *ACS Energy Lett.* **2024**, *9*, 5081–5091.
- (9) Yang, A.; Sun, Y.; Zhang, J.; Wang, F.; Zhong, C.; Yang, C.; Hu, H.; Liu, J.; Lin, X. Enhancing Power Conversion Efficiency of Perovskite Solar Cells through Machine Learning Guided Experimental Strategies. *Adv. Funct. Mater.* **2025**, *35*, No. 2410419.
- (10) Liu, Y.; Tan, X.; Liang, J.; Han, H.; Xiang, P.; Yan, W. Machine Learning for Perovskite Solar Cells and Component Materials: Key Technologies and Prospects. *Adv. Funct. Mater.* **2023**, *33*, No. 2214271.
- (11) Zhi, C.; Wang, S.; Sun, S.; Li, C.; Li, Z.; Wan, Z.; Wang, H.; Li, Z.; Liu, Z. Machine-Learning-Assisted Screening of Interface Passivation Materials for Perovskite Solar Cells. *ACS Energy Lett.* **2023**, *8*, 1424–1433.
- (12) Zhou, Y.; Herz, L. M.; Jen, A. K.; Saliba, M. Advances and Challenges in Understanding the Microscopic Structure-Property-Performance Relationship in Perovskite Solar Cells. *Nat. Energy* **2022**, *7*, 794–807.
- (13) Vaynzof, Y. The Future of Perovskite Photovoltaics-Thermal Evaporation or Solution Processing? *Adv. Energy Mater.* **2020**, *10*, No. 2003073.
- (14) Yang, X.; Luo, D.; Xiang, Y.; Zhao, L.; Anaya, M.; Shen, Y.; Wu, J.; Yang, W.; Chiang, Y.-H.; Tu, Y.; Su, R.; Hu, Q.; Yu, H.; Shao, G.; Huang, W.; Russell, T. P.; Gong, Q.; Stranks, S. D.; Zhang, W.; Zhu, R. Buried Interfaces in Halide Perovskite Photovoltaics. *Adv. Mater.* **2021**, *33*, No. 2006435.
- (15) Li, N.; Niu, X.; Chen, Q.; Zhou, H. Towards Commercialization: The Operational Stability of Perovskite Solar Cells. *Chem. Soc. Rev.* **2020**, *49*, 8235–8286.
- (16) Janjua, M. R. S. A.; Shafiq, Z.; Shahzadi, S.; Rehman, U.; Shoukat, S.; Azeem, R.; Ali, S. H.; Goni, L. K. M. O. Recent Developments and Future Challenges for Perovskite Solar Cells: Physical Insights to Improve Pce. *Braz. J. Phys.* **2024**, *54*, 134.
- (17) Dastgeer, G.; Nisar, S.; Zulfiqar, M. W.; Eom, J.; Imran, M.; Akbar, K. A Review on Recent Progress and Challenges in High-Efficiency Perovskite Solar Cells. *Nano Energy* **2024**, *132*, No. 110401.
- (18) Zhu, M.; Xia, Y.; Qin, L.; Zhang, K.; Liang, J.; Zhao, C.; Hong, D.; Jiang, M.; Song, X.; Wei, J.; Zhang, P.; Tian, Y.; Jin, Z. Reducing Surficial and Interfacial Defects by Thiocyanate Ionic Liquid Additive

- and Ammonium Formate Passivator for Efficient and Stable Perovskite Solar Cells. *Nano Res.* **2023**, *16*, 6849–6858.
- (19) Dong, H.; Ran, C.; Gao, W.; Sun, N.; Liu, X.; Xia, Y.; Chen, Y.; Huang, W. Crystallization Dynamics of Sn-Based Perovskite Thin Films: Toward Efficient and Stable Photovoltaic Devices. *Adv. Energy Mater.* **2022**, *12*, No. 2102213.
- (20) Ma, J.; Qin, M.; Li, P.; Han, L.; Zhang, Y.; Song, Y. Crystallization Kinetics Modulation and Defect Suppression of All-Inorganic  $\text{CsPbX}_3$  Perovskite Films. *Energy Environ. Sci.* **2022**, *15*, 413–438.
- (21) Xu, H.; Zhu, J.; Finegan, D. P.; Zhao, H.; Lu, X.; Li, W.; Hoffman, N.; Bertei, A.; Shearing, P.; Bazant, M. Z. Guiding the Design of Heterogeneous Electrode Microstructures for Li-Ion Batteries: Microscopic Imaging, Predictive Modeling, and Machine Learning. *Adv. Energy Mater.* **2021**, *11*, No. 2003908.
- (22) Park, S. C.; Park, M. K.; Kang, M. G. Super-Resolution Image Reconstruction: A Technical Overview. *IEEE Signal Process Mag.* **2003**, *20*, 21–36.
- (23) Hore, A.; Ziou, D. Image Quality Metrics: PSNR vs. SSIM. In *20th International Conference on Pattern Recognition*; IEEE, 2010; pp 2366–2369.
- (24) Liu, Y. H. In Feature Extraction and Image Recognition with Convolutional Neural Networks. *J. Phys. Conf. Ser.* **2018**, *1087*, No. 062032.
- (25) Peng, X.; Zhang, X.; Li, Y.; Liu, B. Research on Image Feature Extraction and Retrieval Algorithms Based on Convolutional Neural Network. *J. Visual Commun. Image Represent.* **2020**, *69*, No. 102705.
- (26) Martinelli, A. Vision and Imu Data Fusion: Closed-Form Solutions for Attitude, Speed, Absolute Scale, and Bias Determination. *IEEE Trans. Rob.* **2012**, *28*, 44–60.
- (27) Ramachandram, D.; Taylor, G. W. Deep Multimodal Learning: A Survey on Recent Advances and Trends. *IEEE Signal Process Mag.* **2017**, *34*, 96–108.
- (28) Taud, H.; Mas, J.-F. Multilayer Perceptron (Mlp). In *Geomatic Approaches for Modeling Land Change Scenarios*; Springer, 2017; pp 451–455.
- (29) Awad, M.; Khanna, R. Support Vector Regression. In *Efficient Learning Machines: Theories, Concepts, and Applications for Engineers and System Designers*; Springer Nature, 2015; pp 67–80.
- (30) Ke, G.; Meng, Q.; Finley, T.; Wang, T.; Chen, W.; Ma, W.; Ye, Q.; Liu, T.-Y. LightGBM: A Highly Efficient Gradient Boosting Decision Tree. *Adv. Neural. Inf. Process. Syst.* **2017**, *30*.
- (31) Breiman, L. Random Forests. *Mach. Learn.* **2001**, *45*, 5–32.
- (32) Dudani, S. A. The Distance-Weighted K-Nearest-Neighbor Rule. *IEEE Trans. Syst. Man. Cybern.* **1976**, *SMC-6*, 325–327.
- (33) Muscarella, L. A.; Hutter, E. M.; Sanchez, S.; Dieleman, C. D.; Savenije, T. J.; Hagfeldt, A.; Saliba, M.; Ehrler, B. Crystal Orientation and Grain Size: Do They Determine Optoelectronic Properties of  $\text{MAPbI}_3$  Perovskite? *J. Phys. Chem. Lett.* **2019**, *10*, 6010–6018.
- (34) McGovern, L.; Koschany, I.; Grimaldi, G.; Muscarella, L. A.; Ehrler, B. Grain Size Influences Activation Energy and Migration Pathways in  $\text{MAPbBr}_3$  Perovskite Solar Cells. *J. Phys. Chem. Lett.* **2021**, *12*, 2423–2428.
- (35) Ren, X.; Yang, Z.; Yang, D.; Zhang, X.; Cui, D.; Liu, Y.; Wei, Q.; Fan, H.; Liu, S. F. Modulating Crystal Grain Size and Optoelectronic Properties of Perovskite Films for Solar Cells by Reaction Temperature. *Nanoscale* **2016**, *8*, 3816–3822.
- (36) Hu, M.; Bi, C.; Yuan, Y.; Bai, Y.; Huang, J. Stabilized Wide Bandgap  $\text{MAPbBr}_{x}\text{I}_{3-x}$  Perovskite by Enhanced Grain Size and Improved Crystallinity. *Adv. Sci.* **2016**, *3*.
- (37) Xu, J.; Shi, P.; Zhao, K.; Yao, L.; Deger, C.; Wang, S.; Zhang, X.; Zhang, S.; Tian, Y.; Wang, X.; Shen, J.; Zhang, C.; Yavuz, I.; Xue, J.; Wang, R. Ion-Migration Inhibitor for Spiro-Ometad/Perovskite Contact toward Stable Perovskite Solar Cells. *ACS Energy Lett.* **2024**, *9*, 1073–1081.
- (38) Zhang, Y.; He, L.; Cai, Y.; Zhang, J.; Wang, P. Aza [5] Helicene-Derived Semiconducting Polymers for Improved Performance in Perovskite Solar Cells: Exploring Energetic and Morphological Influences. *Angew. Chem., Int. Ed.* **2024**, *63*, No. e202401605.
- (39) Peng, D.; Xia, Z.; Wang, H.; Chen, C.; Zhai, M.; Tian, Y.; Cheng, M. An Efficient Asymmetric Structured Hole Transport Material for Perovskite Solar Cells. *Chem. Commun.* **2024**, *60*, 2665–2668.
- (40) Zhao, Y.; Ma, T.; Liu, T.; Zhou, L.; Wu, Z.; Chen, C.; Liu, Y.; Chen, C.; Ma, D.; Qin, L.; Zhao, D.; Wang, C.; Li, X. Passivator-Assisted Close Space Annealing for High-Performance Wide-Bandgap Perovskite Solar Cells. *Solar RRL* **2024**, *8*, No. 2301016.
- (41) Chen, Q.; Wu, J.; Liu, X.; Du, Y.; Deng, C.; Chen, X.; Sun, L.; Tan, L.; Sun, W.; Lan, Z. Small-Molecule Copper Chloride Modulating the Buried Interfaces of Perovskite Solar Cells. *ACS Appl. Mater. Interfaces* **2024**, *16*, 8949–8959.
- (42) Chen, J.; Liu, J.; Li, Y.; Xu, P.; Xie, L.; Meng, Y.; Wu, H.; Shang, X.; Zhao, S.; Pan, J.; Xiao, C.; Yang, M.; Ge, Z. Ultrasonic-Assisted Processing Combined with Gas Quenching for Fabricating High-Performance and Stable Inverted Perovskite Solar Cells. *Adv. Funct. Mater.* **2024**, *34*, No. 2314652.
- (43) Xie, F.; Huang, C.; Dong, G.; Wu, M.; Wu, K.; Du, S.; Li, Y.; Wei, M. One-Step Hydrothermal Synthesis of Zr-Doped Brookite  $\text{TiO}_2$  Nanorods for Highly Efficient Perovskite Solar Cells. *Mater. Res. Bull.* **2024**, *173*, No. 112677.
- (44) Kwon, N.; Seo, J. Functionalized Polymer-Capped  $\text{SnO}_2$  Nanoparticle Electron Transport Layer for Efficient Perovskite Solar Cells. *Korean J. Chem. Eng.* **2024**, *1*–10.
- (45) Cheng, N.; Li, W.; Zheng, D.; Yang, W. X. Enhance the Efficiency of Perovskite Solar Cells Using W Doped  $\text{SnO}_2$  Electron Transporting Layer. *ChemPhotoChem.* **2024**, *8*, No. e202300275.
- (46) Li, T.; Zhang, Y.; Ren, M.; Mu, Y.; Zhang, J.; Yuan, Y.; Zhang, M.; Wang, P. Triisocyanate Derived Interlayer and High-Melting-Point Doping Promoter Boost Operational Stability of Perovskite Solar Cells. *Angew. Chem., Int. Ed.* **2024**, *63*, No. e202401604.